Mechanosynthesis of polymer-stabilized lead bromide perovskites: Insight into the formation and phase conversion of nanoparticles

Guocan Jiang[1], Onur Erdem[2], René Hübner[4], Maximilian Georgi[1], Wei Wei[1], Xuelin Fan[1], Jin Wang[5], Hilmi Volkan Demir[2,3], and Nikolai Gaponik[1] (✉)

[1] *Physical Chemistry, Technische Universität Dresden, Zellescher Weg 19, 01069 Dresden, Germany*
[2] *Department of Physics, Department of Electrical and Electronics Engineering, and UNAM – Institute of Materials Science and Nanotechnology, Bilkent University, 06800 Ankara, Turkey*
[3] *LUMINOUS! Center of Excellence for Semiconductor Lighting and Displays, School of Electrical and Electronic Engineering, School of Mathematical and Physical Sciences, School of Materials Science and Engineering, Nanyang Technological University, Nanyang Avenue, Singapore 639798, Singapore*
[4] *Helmholtz-Zentrum Dresden-Rossendorf, Institute of Ion Beam Physics and Materials Research, Bautzner Landstrasse 400, 01328 Dresden, Germany*
[5] *Key Laboratory of the Ministry of Education for Advanced Catalysis Materials, Zhejiang Normal University, Jinhua 321004, China*

ABSTRACT

The application of polymers to replace oleylamine (OLA) and oleic acid (OA) as ligands for perovskite nanocrystals is an effective strategy to improve their stability and durability especially for the solution-based processing. Herein, we report a mechanosynthesis of lead bromide perovskite nanoparticles (NPs) stabilized by partially hydrolyzed poly(methyl methacrylate) (h-PMMA) and high-molecular-weight highly-branched poly(ethylenimine) (PEI-25K). The as-synthesized NP solutions exhibited green emission centered at 516 nm, possessing a narrow full-width at half-maximum of 17 nm and as high photoluminescence quantum yield (PL QY) as 85%, while showing excellent durability and resistance to polar solvents, e.g., methanol. The colloids of polymer-stabilized NPs were directly processable to form stable and strongly-emitting thin films and solids, making them attractive as gain media. Furthermore, the roles of h-PMMA and PEI-25K in the grinding process were studied in depth. The h-PMMA can form micelles in the grinding solvent of dichloromethane to act as size-regulating templates for the growth of NPs. The PEI-25K with large amounts of amino groups induced significant enrichment of $PbBr_2$ in the reaction mixture, which in turn caused the formation of $CsPb_2Br_5$-$mPbBr_2$ and $CsPbBr_3$-Cs_4PbBr_6-$nCsBr$ NPs. The presence of $CsPbBr_3$-Cs_4PbBr_6-$nCsBr$ NPs was responsible for the high PL QY, as the Cs_4PbBr_6 phase with a wide energy bandgap can passivate the surface defects of the $CsPbBr_3$ phase. This work describes a direct and facile mechanosynthesis of polymer-coordinated perovskite NPs and promotes in-depth understanding of the formation and phase conversion for perovskite NPs in the grinding process.

KEYWORDS

lead bromide perovskites, mechanosynthesis, polymer ligands, polymer micelles, poly(ethyleneimine)-induced phase conversion

1   Introduction

Owing to their broadly tunable photoluminescence (PL) across 400–700 nm, narrow PL full-width at half-maxima (FWHM) of 12–40 nm for a blue-to-red spectral region, and high PL quantum yields (QYs) of 50%–90%, all-inorganic $CsPbX_3$ (X = Cl, Br, or I) perovskite nanoparticles (NPs) have attracted tremendous interest especially in photonic applications [1, 2], including electrically-driven light-emitting diodes (LEDs) [3, 4], color-conversion white LEDs (WLEDs) [5, 6], lasers [7, 8], and X-ray scintillators [9, 10]. Furthermore, the relatively low formation energy and high defect tolerance of these lead-halide perovskites enable the synthesis of their highly fluorescent nanocrystals via relatively simple synthetic procedures at low-temperature [11–13]. However, the labile surface, ionic nature, and metastable structure of perovskite materials cause them

to suffer from poor stability and durability, especially in the solution-processing steps [14, 15]. For example, the process of precipitation and concentration of perovskite NPs using polar solvents is often accompanied by a large decrease in PL QY due to the loss of dynamic oleylamine (OLA) and oleic acid (OA) ligands [15]. Additionally, strong polar solvents, such as methanol and ethanol, will completely quench the fluorescence of OLA/OA-capped perovskite nanocrystals [14].

To improve the stability of perovskites, previous reports focused on the following three strategies: (i) modification of the OLA/OA-capped perovskite surface with stronger binding ligands [14–19]; (ii) encapsulation of perovskite materials into inorganic oxides [20–25] or hydrophobic polymers [5, 23, 26]; and (iii) construction of various composite heterostructures with different perovskite phases [6, 27–32]. The relatively weak interactions between perovskite nanocrystal and OLA/OA

opened up many opportunities for further surface design and modification [15, 33]. Ligands, such as zwitterionic molecules [14], benzenesulfonic acid [15], didodecyl dimethylammonium bromide (DDAB) [16], phosphine ligands [17, 19], and 2,2'-iminodibenzoic acid (IDA) [18] with stronger binding to the nanocrystal surface were used to enhance the PL QY as well as the durability and resistance to polar solvents of the nanocrystals. Generally, most of the inorganic oxides, such as silsesquioxane [23, 25], SiO_2 [21, 24], AlO_x [20, 24], and glass [22], can physically isolate the perovskite materials from the surrounding chemical environment, thus significantly improving their stability. However, this isolation is often accompanied by a significant reduction in solution processability for encapsulated materials. Some hydrophobic polymers, such as polyvinylidene fluoride (PVDF) [5], poly(methyl methacrylate) (PMMA) [23], and polystyrene (PS) [26], can not only play a role similar to inorganic oxides, but also impart excellent solution processability, which is very favorable for solution-processable applications.

As solely the $CsPbBr_3$ phase exhibits high PL among many other known phases of cesium lead halide perovskites [34, 35], the stability of this phase may not only be improved by its embedding in a foreign robust material, but also by combining it with other non-fluorescent phases of the perovskite family, such as Cs_4PbBr_6, and $CsPb_2Br_5$. Indeed, the relatively stable light-emitting heterostructures of core-shell $CsPbBr_3/Cs_4PbBr_6$ [29], $CsPbBr_3$ embedded in Cs_4PbBr_6 [6, 28], $CsPbBr_3$ blended with Cs_4PbBr_6 [27, 31], and $CsPbBr_3$ blended with $Cs_2Pb_2Br_5$ [30, 32] were reported. In addition to the positive influence on the stability, these $Cs_2Pb_2Br_5$ and Cs_4PbBr_6 phases with wide energy bandgap can passivate surface defects of the $CsPbBr_3$ phase, thus improving its PL QY. This kind of heterostructures are of special practical interest, as they may be created by relatively versatile and easily up-scalable methods (e.g., one-pot synthesis) by utilizing a limited amount of precursors. Moreover, the in-depth investigation of these heterostructures of various designs is very helpful for understanding the mechanisms of both radiative and non-radiative processes in the $CsPbBr_3$ phase.

In our recent work, we reported that the $CsPbBr_3$-$CsPb_2Br_5$ NPs coordinated by partially hydrolyzed PMMA (h-PMMA) and low-molecular-weight (800 g/mol) poly(ethylenimine) (PEI-0.8K) exhibited impressive water and UV resistance as well as thermal stability while maintaining high PL QY [36]. We attributed this attractive improvement to the synergetic influence of the surface modification with strong binding ligands, polymer-encapsulation, and proper heterostructuring of the emitting and non-emitting perovskite-phases.

Herein, attempting to further understand and master this system, we performed systematic in-depth investigations and found that although addition of the highly branched PEI improved the PL QY, the system investigated did not tolerate further increasing of the PEI-0.8K content and reached its limits by the concentrations reported in [36]. The application of a high-molecular-weight (25,000 g/mol) PEI (further referred to as PEI-25K) ligand in the NP synthesis allowed us to overcome this limitation. Moreover, the systematic investigations reported here show that the application of this new ligand in combination with h-PMMA results not only in the improvement of the PL QY of the perovskite NPs, but has also a significant effect on the morphology, phase composition, and spectrum of the resulting materials. The improvement of the luminescence is not incremental, as it is based on the phase transformation of the shelling structure of the emitting centers from originally $CsPbBr_3$-$CsPb_2Br_5$ to $CsPbBr_3$-Cs_4PbBr_6-$nCsBr$. The as-prepared NP solutions emit green light peaked at 516 nm; the PL is narrow

(FWHM of 17 nm) and strong (PL QY of 85%). Moreover, they exhibit excellent durability and resistance to methanol—the solvent typically used for processing colloidal NPs. Based on the results of the comprehensive characterization techniques, we clarified the roles of the h-PMMA and PEI-25K during the synthesis and confirmed the chemical composition and the structure of both the intermediate and final reaction products obtained under influence of the PEI. Finally, the resultant NPs were successfully utilized as a gain medium for amplified spontaneous emission (ASE), which is an example application in solution-processable optoelectronics.

2 Results and discussion

Perovskite NPs stabilized by h-PMMA/b-PEI were prepared based on our previous work with some modifications [36]. Specifically, mixtures of equivalent molar amounts of $PbBr_2$ and CsBr were ground by a ball mill. The appearance of a yellow powder indicated the formation of bulk $CsPbBr_3$. Next, the polymer of h-PMMA with a 10% degree of hydrolysis and PEI-25K dissolved in dichloromethane (DCM) were added and the mixture was subjected to further grinding. The resulting product was further diluted and collected with DCM. After centrifugation, the DCM-supernatant was replaced with pure toluene allowing to obtain toluene solutions of NPs. Our previous work showed that the amount of PEI had a significant effect on the morphology and optical properties of the resultant NPs, while the amount of h-PMMA did not. Therefore, in the present work, we fixed the amount of h-PMMA in grinding at 0.1 g and studied the effect of various amounts of PEI-25K (0, 0.01, 0.015, 0.02, 0.025, and 0.03 g) on the properties of the NPs.

2.1 Morphology and composition

The typical h-PMMA-capped NPs exhibit a cubic shape with a uniform size of 29.3 ± 6.1 nm (Fig. 1(a)), an elemental ratio of Cs:Pb:Br = 1.0:1.1:2.9 (Fig. 1(a)) and the orthorhombic phase of $CsPbBr_3$ (Fig. 1(g)). The introduction of PEI causes the resulting NPs to change from cubes to larger spheres of a less regular size. Spots with a stronger contrast can be recognized in the transmission electron microscopy (TEM) images of the individual spheres (Figs. 1(b)–1(f)). As the amount of PEI added to the synthesis increases, X-ray diffraction (XRD) peaks corresponding to the $CsPbBr_3$ phase gradually diminish, as shown in Fig. 1(g) and Fig. S2 in the Electronic Supplementary Material (ESM). Simultaneously, the relative intensity of the diffraction peaks of Cs_4PbBr_6 and CsBr gradually increases (Fig. 1(g)). These changes are accompanied by the appearance of an unspecific background, which could be associated with an amorphous phase (Fig. S2 in the ESM). The resulting NPs modified by 0.03 g of PEI show the dominating diffraction peaks of the crystal phases of Cs_4PbBr_6 and CsBr with almost completely disappeared signals related to $CsPbBr_3$ (Fig. 1(g)). Meanwhile, the elemental ratio of Pb and Br relative to Cs in the resulting NPs increased first, reached its maximum (Cs:Pb:Br = 1.0:10.1:19.7) at the PEI amount of 0.025 g, and decreased again with the higher concentrations of PEI added (Fig. S3 and Table S1 in the ESM). As will be shown below, the NPs synthesized in the presence of 0.025 g of PEI-25K possess the highest PL QY of 85% among all considered samples. The majority of these NPs appear in TEM as uniform spherical particles containing many spots of a higher contrast material. Three crystal phases of $CsPbBr_3$, Cs_4PbBr_6, and CsBr, as well as amorphous phases are evidenced in this sample by powder XRD. The elemental ratio is found to be Cs:Pb:Br = 1.0:10.1:19.7.
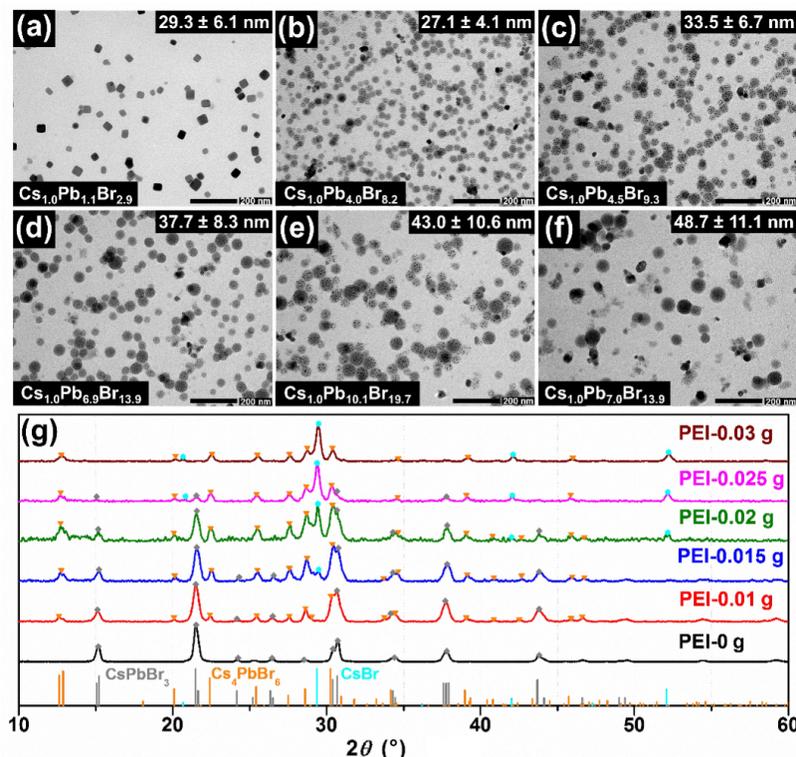
Figure 1 Morphology and composition of the NPs obtained using different PEI-25K additions and a fixed amount of h-PMMA (0.1 g). Panels (a)–(f) show the NPs with PEI amounts of 0, 0.01, 0.015, 0.020, 0.025, and 0.030 g, respectively. Elemental composition and average particle size are inserted in the lower left and upper right corners of the corresponding images, respectively. The detailed size-distribution diagrams are provided in Fig. S1 in the ESM. (g) Powder XRD data of the corresponding samples with subtracted background. The raw XRD data are shown in Fig. S2 in the ESM. The standard diffraction peaks of $CsPbBr_3$, Cs_4PbBr_6, and CsBr are taken from C18-364, PDF#73-2478 and C5-588, respectively.

2.2 Formation and phase conversion of the nanoparticles

Based on the above description of the morphology and phase composition, the following questions are especially worth of further discussion: i) Why do these NPs prepared by ball milling exhibit such uniform size? and ii) what exactly are the particles observed in the bright-field TEM images? In order to address these questions, a representative sample synthesized with 0.025 g PEI-25K was further characterized by high-angle annular dark-field scanning transmission electron microscopy (HAADF-STEM) imaging combined with element mapping based on energy dispersive X-ray spectroscopy (EDX) analysis to determine the composition of the individual particles. As shown in Figs. 2(a)–2(c) and Figs. S4(a)–S4(c) in the ESM, approximately 15% of the NPs (highlighted by blue circles) are characterized by a Cs-rich and Pb/Br/N-deficient elemental composition. The rest of the particles exhibit a Cs-deficient and Pb/Br/N-rich elemental composition. Furthermore, high-resolution TEM imaging was carried out to test the crystallinity of the NPs. While there are no indications for lattice fringes in the case of the Cs-deficient particles pointing to their amorphous nature, lattice arrangements are observed for the Cs-rich NPs, which are hence crystalline (Fig. 2(d)). The crystal lattice parameters match the lattice parameters of three phases, namely CsBr, Cs_4PbBr_6, and $CsPbBr_3$ (Fig. S5 in the ESM). It is worth mentioning that the spots of stronger contrast observed within the Cs-deficient particles (Fig. 1(e)) and pointing to the presence of Pb decompose during intense electron illumination; hence, these spots are not visible in the high-resolution TEM and HAADF-STEM micrographs as well as the element maps (Fig. 2). Based on the comparative analysis of the results provided by XRD and electron microscopy, we propose a possible mechanism of the formation and phase transformation of these particles during grinding, which is discussed below and schematically

presented in Fig. 2(g) and Fig. S6 in the ESM.

After adding h-PMMA/PEI solved in DCM to the milling jar, most h-PMMA remains in the solvent phase of DCM; however, most PEI bounds quickly to $PbBr_2$ in the solid phase, which is expected considering the different binding forces between the corresponding polymer (h-PMMA or PEI) and the solid phase [36, 37]. The h-PMMA may form micellar templates for the growth of NPs due to the interactions between the hydrophobic ester bond and hydrophilic carboxylic acid group (or carboxylic acid anion) in the non-polar DCM. A possible formation of micelles in the polymer solutions in DCM was monitored by the Tyndall experiment and by dynamic light scattering (DLS) measurements (Fig. S7 in the ESM). The solution of conventional non-hydrolyzed PMMA appeared completely transparent for the laser beam. The obvious formation of scattering particles was evidenced in the DCM solutions of h-PMMA and h-PMMA/PEI. Moreover, the DLS results show a higher degree of aggregation of the polymeric phase upon the introduction of PEI; in other words, micelles of a bigger average size could be formed. Thus, the reason for the increase in particle size of the resulting NPs may partly be attributed to the fact that after PEI introduction the negatively charged carboxylate from h-PMMA causes assembling into larger micelles.

As the direct *in situ* observation of the micelles formed during the milling process is impossible and considering the influence of heat and uneven distribution of PEI on micelle assembly behavior in the milling reactor is cumbersome, the results of the Tyndall and DLS experiments can only provide indirect evidence for the origin of micelle formation. In addition, a control experiment of grinding exactly the same precursors in absence of h-PMMA was carried out. In this case, we failed to obtain the colloidal solution of perovskite NPs (Fig. S7(c) in
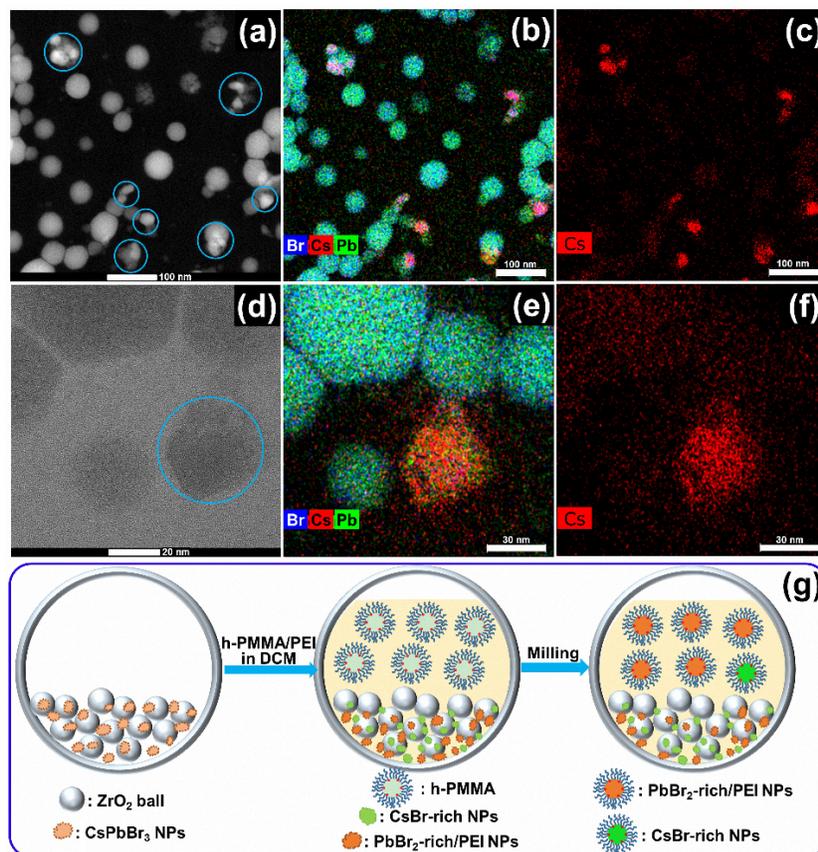
Figure 2 TEM-based characterization of the NPs obtained using additions of 0.025 g PEI-25K and 0.1 g h-PMMA. (a) Overview HAADF-STEM image of h-PMMA/PEI-capped NPs and corresponding element maps based on EDX analysis: (b) Superposition of Cs, Pb, Br and (c) Cs only. (d) High-resolution TEM image of h-PMMA/PEI-capped NPs and corresponding element maps: (e) Superposition of Cs, Pb, Br and (f) Cs only. (g) Schematic diagram of the proposed NPs formation process.

the ESM). The resulting powder particles are in the size range of micrometers (Fig. S7(d) in the ESM), which is expected and consistent with literature reports [38, 39]. In its own turn, the nano-sized perovskite NPs can be prepared in the presence of h-PMMA as shown in Fig. 1(a). The analysis of the above measurements allow us to suggest that the uniform size of NPs prepared by grinding can be attributed to the h-PMMA micellar templates formed in DCM. The micellar fabrication of various nanocrystals is well known and was successfully applied to the synthesis of $CsPbBr_3$ by Yoon et al. [40, 41]. In those works, the authors used star-like PAA-b-PS nanoreactors to obtain monodisperse particles with solution-based synthesis.

The highly branched PEI, which is rich in amino-groups (about 600 amino groups per PEI-25K molecule), could form a complex with $PbBr_2$ in solid phase, due to the strong interaction between the vacant orbital from Pb^{2+} and the lone electron pair of nitrogen from PEI [36, 37]. This complexation will further result in the redistribution of the material in the reaction mixture into the $PbBr_2$-rich phase of $CsPbBr_3$-$xPbBr_2$/PEI and the rest, i.e., the CsBr-rich phase of $CsPbBr_3$-$yCsBr$, in accordance to Reaction (1)

$$CsPbBr_3 \text{ (solid)} + PEI \rightarrow$$
$$CsPbBr_3\text{-}xPbBr_2/PEI \text{ (in solid)} + CsPbBr_3\text{-}yCsBr \text{ (in solid)} \quad (1)$$
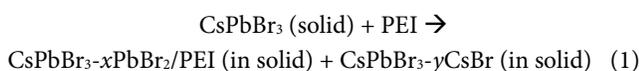
The values of x and y in Reaction (1) reflect an additive influence of both the molecular weight and the amount of PEI molecules. Thus, these values are expected to be relatively high if the high-molecular-weight PEI-25K is used as compared to the case when the low-molecular-weight PEI-0.8K was used, as we did in our previous report [36]. Of particular note, the

value of x should be significantly higher than the value of y, since PEI-25K can only enrich $PbBr_2$ but not CsBr. Both phases formed in Reaction (1) can undergo further transformations under the conditions considered here. The $CsPbBr_3$-$xPbBr_2$/PEI phase can further convert to $CsPb_2Br_5$-$mPbBr_2$/PEI based on Reaction (2)

$$CsPbBr_3\text{-}xPbBr_2/PEI \rightarrow CsPb_2Br_5\text{-}mPbBr_2/PEI \quad (2)$$

This phase conversion is well expected due to the low binding energy of perovskite materials. It is worth noting that if the molecular weight or amount of PEI added is very low, resulting in a small value of x, the final product of the reaction should be $CsPbBr_3$-$CsPb_2Br_5$/PEI, which is in agreement with our previous work [36]. The $CsPbBr_3$-$yCsBr$ phase in its own turn can spontaneously be converted to $CsPbBr_3$-Cs_4PbBr_6-$nCsBr$ based on Reaction (3)

$$CsPbBr_3\text{-}yCsBr \rightarrow CsPbBr_3\text{-}Cs_4PbBr_6\text{-}nCsBr \quad (3)$$

It should be noted that m and n used in Reactions (2) and (3), respectively, are parameters representing some arbitrary fraction of the coefficients x and y in Reaction (1), which are ultimately determined by the amount of PEI added and its molecular weight. Under high-speed shaking and milling, the above two products formed in Reactions (2) and (3) could enter into the solution to form colloidal particles coordinated with h-PMMA ligand through the interaction of carboxyl or carboxylate and Pb^{2+}, as illustrated in the diagram of Fig. 2(g). However, compared to $CsPbBr_3$-Cs_4PbBr_6-$nCsBr$ particles, the particles of $CsPb_2Br_5$-$mPbBr_2$/PEI can provide more binding sites for the coordination with h-PMMA; therefore the product of

Reaction (2) will enter into solution with a higher rate and the NPs of $CsPb_2Br_5$-$m$$PbBr_2$/PEI coordinated with h-PMMA become a major colloidal product. On the other hand, a relatively small amount of $CsPbBr_3$-Cs_4PbBr_6-$n$$CsBr$ NPs can enter into colloidal solution, which makes them a minor product of the reaction.

One more side reaction, which is necessary to complete the picture, should be mentioned here. $PbBr_2$ available in the product of Reaction (2) can be reduced to Pb^0 by amino groups of the PEI-25K under the heating caused by the high-speed milling [42, 43]

$$PEI-NH_2 + \tfrac{1}{2}PbBr_2 \rightarrow PEI-NH_2^+ \cdot Br^- + \tfrac{1}{2}Pb^0 \qquad (4)$$

For simplicity, we normalized the reaction stoichiometry to a single amino-group. It is, however, clear that the highly branched PEI contains plenty of amino entities available for this reaction. We attribute the spots of a higher contrast material observable inside of the spherical nanoparticles in Fig. 1(e) to the metallic Pb formed in Reaction (4) [42, 43]. Diffraction peaks of neither Pb nor $PbBr_2$ and $CsPb_2Br_5$ phases can be recognized in powder XRD patterns (Fig. 1(g)). This observation may reflect the formation of amorphous phases or solely very small crystallites of these materials under conditions of binding to the polymer of high molecular weight and branched PEI-25K [44, 45].

The results of this part can thus be summarized as follows: if h-PMMA is the only ligand applied in the synthesis, the above-described phase conversions are not observable. The $CsPbBr_3$ NPs in solid phase enter into DCM to become the only colloidal product after combination with h-PMMA. Therefore, the resultant NPs capped by h-PMMA show the perovskite phase, a cubic shape, and an element composition corresponding to $CsPbBr_3$ (Figs. 1(a) and 1(g)). The introduction of PEI triggers the above-listed series of phase transition reactions resulting in the appearance of two colloidal products, namely the major amorphous product of $CsPb_2Br_5$-$m$$PbBr_2$ particles coordinated with PEI/h-PMMA and the minor crystalline product of $CsPbBr_3$-Cs_4PbBr_6-$n$$CsBr$ particles coordinated with h-PMMA. Increasing the amount of the branched PEI added to the reaction causes the preferable formation of h-PMMA-capped $CsPb_2Br_5$-$m$$PbBr_2$/PEI NPs. This was reflected by the gradual increase in the elemental ratio of Pb and Br in the final product (Figs. 1(a)–1(f)).

2.3 Spectral characterization

The NPs obtained with different amounts of PEI (0, 0.01, 0.015, 0.020, 0.025, and 0.030 g) were characterized by optical spectroscopy. The NPs obtained with solely h-PMMA as ligand exhibit a typical absorption spectrum of $CsPbBr_3$ NPs. Furthermore, they show a narrow PL with a FWHM of about 16 nm peaking at 518 nm with a QY of 8.2%, (Fig. 3 and Table S2 in the ESM).

After the introduction of PEI-25K, the strong absorption peaks appearing at 290–320 nm indicate the occurrence of non-$CsPbBr_3$ phases for the resulting NPs. This is accompanied by a slight blue shift of the PL maximum (about 2 nm) and the significant increase of the PL QY. Based on the phase conversion mechanism discussed above, it can be concluded that both Cs-rich and $PbBr_2$-rich particles could contribute to the PL, if the amount of PEI added to the system is relatively low (e.g., around 0.01 g). As followed from the Reaction (2), the $PbBr_2$-rich particles are expected to consist of $CsPbBr_3$-$CsPb_2Br_5$/PEI with this amount of PEI. If the amount of PEI added is higher (i.e., 0.015 g or more), the $PbBr_2$-rich phase consists of $CsPb_2Br_5$-$m$$PbBr_2$ and could not contribute to the emission. In this case, solely the emission from the CsBr-rich NPs, namely the

$CsPbBr_3$-Cs_4PbBr_6-$n$$CsBr$ obtained according to the Reactions (1) and (3) is observed. The slight deviations in the PL peak positions may reflect the deviations in average particle sizes.

Moreover, the significant increase of the PL QYs should result from the wide energy bandgap of Cs_4PbBr_6 improving the carrier confinement in the $CsPbBr_3$ phase and suppressing its surface defects [6, 28]. The optical absorption in the spectral region of 460–520 nm is associated with $CsPbBr_3$ phase [34, 35]. Although, the absolute quantification of these data is complicated due to the uncertainty of the extinction coefficient of the NPs, the relative analysis is well applicable. Indeed, with increasing amount of the PEI-25K added to the synthesis, this absorption feature diminishes, indicating a decrease of the relative amount of $CsPbBr_3$ phase (Fig. 3(a)). Thus, in order to obtain strongly emitting NPs, the amount of the PEI added to the system should be carefully optimized. In this work, the NPs modified by 0.025 g of PEI-25K were found to consist of a balanced amount of about 15% of $CsPbBr_3$-Cs_4PbBr_6-$n$$CsBr$ fluorescent phase, allowing this sample to exhibit the highest PL QY of 85%. The fluorescence decay measurements show that, upon the introduction of PEI-25K, the fluorescence lifetime of the resulting NPs increases (from 8.4 to 15.0 ns) (Fig. 3(d) and Table S2 in the ESM). This may be the result of the combined effects of both the change in particle size of the $CsPbBr_3$ phase and the passivation of the $CsPbBr_3$ surface by the Cs_4PbBr_6 phase [28, 36].

To demonstrate the versatility of our approach and its applicability to obtain NPs with other emission colors, blue- and red-emitting NPs were prepared by ion-exchange reactions. To this end, the NPs prepared with 0.025 g of PEI-25K were treated with $ZnCl_2$ and ZnI_2 dissolved in CH_3OH, respectively. True-color images, absorption and PL spectra of the resulting NPs are shown in Fig. S8 in the ESM, and the corresponding spectral data are summarized in Table S3 in the ESM. The deep blue-emitting NPs exhibit a PL peak at 456 nm, a narrow FWHM of ~ 12.9 nm, and a PL QY of 28%, while the red-emitting NPs are characterized by a PL peak at 641 nm with a larger FWHM of ~ 38.6 nm and a PL QY of 32%. The decrease in the PL QY after ion exchange is consistent with
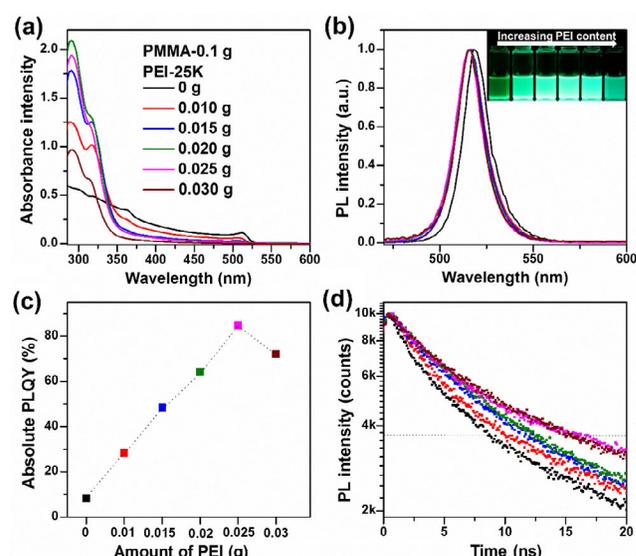

Figure 3 Spectral characterizations of the resulting NPs using different PEI-25K additions (0, 0.01, 0.015, 0.02, 0.025, 0.03 g) and a fixed amount of h-PMMA (0.1 g). (a) Absorbance and (b) PL spectra, (c) PL QY, and (d) PL decay. The dashed line in panel (d) indicates the 1/e'th level of the peak photon count. Inset of panel (b) shows a photograph of the NPs solutions illuminated under 365 nm radiation.

previously reported works [46, 47], which may be due to relatively poor defect tolerance of the chloride-based and iodine-based perovskites [12].

2.4 Stability and durability during solution-based processing

Our previous work indicated that the dual-ligand system of h-PMMA and PEI significantly improves the water resistance, thermal and UV stability of perovskite materials [36]. In the present work, we extended these investigations to the stability in polar solvents and the durability during the precipitation/ redispersion steps. Such kind of treatments are typical, if a colloidal material is subjected to solution-processing technologies (e.g., spin- or dip-coating, casting, spraying or ink-jet printing). Because of the ionic nature of perovskites and their weak-binding to OLA/OA, a strong-polarity solvent, such as methanol or ethanol, can cause the decomposition of perovskite NPs and a substantial loss of the capping ligands accompanied by the complete quenching of the PL [14, 15]. However, the NPs prepared and stabilized by polymer show a high resistance to methanol (Figs. 4(a) and 4(b)). The NP solutions still maintain 65% of their original PL intensity after replacing half of the toluene solvent with methanol (Fig. 4(b)). The fluorescence intensity of the resulting methanol-containing NP solutions was reasonably stable during at least seven days of storage (Fig. S9 in the ESM). This high degradation resistance is provided by the protective layer formed by the hydrophobic PMMA [48], whereas the partial deterioration of the PL may be caused by the weakening of the coordination ability of the PEI in methanol. For OA/OLA-coordinated perovskite NPs, it is common to use polar solvents, such as acetone and n-butanol in combination with high-speed centrifugation to precipitate them. This procedure is applied for "washing" colloidal particles, changing solvent, or increasing their concentration and is often accompanied by the loss of capping OLA, which in turn causes a significant decrease in the PL QY (Fig. 4(c)). Since h-PMMA impart the NPs an obviously different level of solubility as compared to OLA/OA-capped NPs, the former particles can be precipitated without using polar solvents and high-speed centrifugation. The destabilization of the colloidal solution may be achieved in this case by the addition of another non-polar solvent, e.g., n-hexane. More importantly, such a simple method of NP-concentrating is also very robust in that it does not lead to a decrease in PL QY (Figs. 4(c) and 4(d)). After seven times of precipitation with n-hexane and redispersion in toluene, the PL QY of the NPs coordinated by polymer hardly changes as shown in Fig. 4(c). For comparison, regular OLA/OA-capped strongly emitting perovskite NPs were prepared according to the literature [14, 15], and their PL QY was monitored after each cycle of precipitation/redispersion with the polar solvent ethyl acetate. The PL QY of this reference sample decreases from the original 85% to 10% at the end of the 7th precipitation step, owing most likely to the loss of the weakly-binding OLA. The NP-polymer precipitates obtained here exhibit excellent processability imparted by the polymer-ligand. The NP-polymer film appears transparent and greenish, due to the strong PL, which is visible even under ambient light. The samples are also strongly luminescent under UV excitation (Figs. 4(d) and 4(e)). Predictably, the NP-polymer films show excellent storage stability due to the water-resistance of PMMA.

2.5 Amplified spontaneous emission

The h-PMMA/PEI-capped NPs exhibit a high PL QY, excellent stability, and good processability, all together making them attractive for optical applications, especially for solution-based
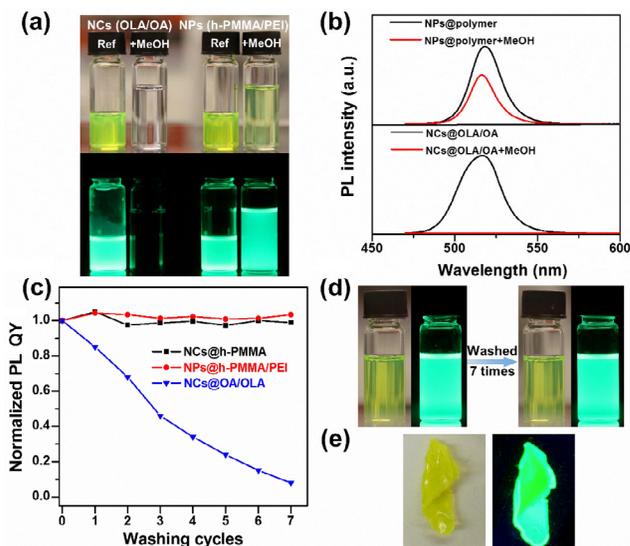

Figure 4 Anti-methanol durability and processability of resulting materials. (a) Photographs of OLA/OA-capped and h-PMMA/PEI-capped NPs solutions before and after addition of methanol. (b) The corresponding change in PL intensity after addition of methanol into both solutions. (c) Normalized PL QY of NPs coordinated with different ligands after 7 cycles of precipitation/redispersion. (d) Images of polymer-NPs after 7 cycles of purification. (e) NPs–polymer composite under air and UV light excitation (at 365 nm).

processing. Here, we demonstrate ASE to show the capability of these NPs to be used for lasing. The ASE can be readily achieved from the h-PMMA/PEI-capped NPs film under femtosecond laser excitation at 400 nm (see Experimental Section). The dynamics of optical gain in the PMMA/PEI-capped NPs film was measured under stripe excitation geometry [49].

As the pump fluence is increased, a second emission feature emerges, which is attributed to ASE (Fig. 5(a)), as evident by its much narrower FWHM (~ 6.2 nm) at room temperature in comparison to that of the spontaneous emission feature (~ 17 nm) as well as a superlinear increase in the output intensity (Fig. 5(b)). The ASE peak is red-shifted by 16 nm with respect to the spontaneous emission peak, suggesting attractive multiexcitonic interaction within these NPs. The emission intensity versus the pumping fluence is plotted in Fig. 5(b), from which an ASE threshold of 18.9 μJ/cm^2 can be extracted. In addition, the pump-dependent gain coefficient for the sample has been determined via the variable stripe length technique [49, 50] at various pump intensities. Figure 5(c) shows the emission intensity at the ASE peak wavelength (~ 534 nm) for various stripe lengths. Accordingly, for a homogeneously excited stripe of length l, the total emission is given by Eq. (5)

$$I = \frac{I_0}{g}(e^{gl} - 1) \tag{5}$$

where I_0 is the spontaneous emission constant. The net gain coefficients extracted from the data in Fig. 5(c) are presented in Fig. 5(d) as a function the of the pump fluence. The net gain coefficient can be expressed as

$$g = A\frac{W_p}{1 + W_p / W_s} - \alpha \tag{6}$$

where A is a constant proportional to the stimulated emission cross-section, W_p is the excitation pump intensity, W_s is the saturation pump intensity, and α is the loss coefficient. The data in Fig. 5(d) are seen to fit well to Eq. (6). We therefore determine the saturation intensity to be $W_s = 73.5$ μJ/cm^2 and
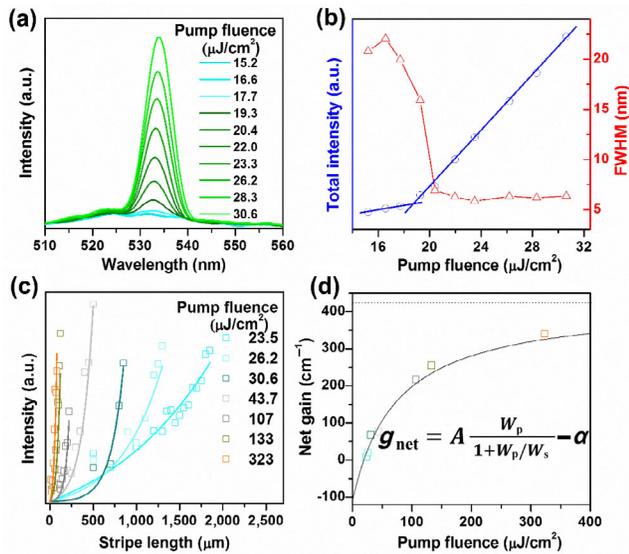
Figure 5 ASE of h-PMMA/PEI-capped NPs film. (a) Emission spectra of h-PMMA/PEI NPs film with increasing excitation fluence. (b) Integrated emission intensity (blue circles) and FWHMs of the emission spectra (red triangles) as a function of the pump energy density. (c) Variable stripe length (VSL) measurements on the h-PMMA/PEI-capped NPs film. PL intensity at the ASE peak (534 nm) as a function of the stripe length for different pump fluences. (d) Extracted net gain coefficients from the data in panel (c). From the fitting in Eq. (6), the saturation intensity is found to be 73.6 μJ/cm^2 and the loss coefficient ~ 110 cm. The net saturated gain is ~ 425 cm^{-1} (dashed line).

the loss coefficient to α = 110 cm^{-1}. The net gain coefficient asymptotically approaches to 425 cm^{-1}, which is thus determined as the saturated gain coefficient.

We note that the ASE threshold achieved by the resulting PMMA/PEI-capped NPs film is lower than previous results reported in the literature [51]. Furthermore, ASE is observed only for the samples with a high-enough density of NPs. In this respect, the polymer ligands inevitably introduce separation between individual NPs, thereby reducing their density, which might be limiting the optical gain coefficient and increasing the gain threshold. This means that our gain medium made of these NPs can potentially be further optimized by tuning the composition, molecular weight, and amount of polymers used for the capping in order to control the inter-particle distance. The successful demonstration of ASE in this work shows that our PMMA/b-PEI-capped NPs possess a great potential as stable and processable luminescent materials in such optical gain media.

3 Conclusion

High molecular weight PEI-25K and h-PMMA were used as double ligands in the preparation of perovskite NPs by milling. The roles of h-PMMA and PEI-25K in the grinding process were studied in depth. The h-PMMA forms micelles in DCM to act as templates for uniform NP growth, whereas high-molecular-weight PEI-25K induces significant enrichment of PbBr$_2$ during the milling process, which in turn causes the formation of CsPb$_2$Br$_5$-mPbBr$_2$ and CsPbBr$_3$-Cs$_4$PbBr$_6$-nCsBr phases. The obtained CsPbBr$_3$-Cs$_4$PbBr$_6$-nCsBr NPs are responsible for the high PL QY of the resulting NP-polymer solutions and solid composites, since the Cs$_4$PbBr$_6$ phase with a wide band gap energy can passivate the surface defects of the emitting CsPbBr$_3$ phase. The as-prepared NPs solutions exhibit green emission peaking at 516 nm, possess a narrow FWHM of 17 nm, and maintain a high PL QY of 85%. More importantly,

the resulting NP solutions possess excellent durability and resistance to methanol as well as offer solution-based processability, making them attractive as solution-processable optical gain media. This work provides new insights in the preparation of uniformly sized perovskite nanoparticles by grinding and sheds light on the mechanism of a phase conversion happening with such perovskite materials under grinding and influence of an amino-group rich medium.

4 Experimental section

4.1 Preparation of perovskite nanoparticles

PMMA possessing a degree of hydrolysis of 10% (h-PMMA) was prepared based on our previous work [36]. The perovskite NPs were prepared by mechanical grinding as follows. PbBr$_2$ (73.4 mg, 0.2 mmol) and CsBr (42.4 mg, 0.2 mmol) were loaded under ambient atmosphere into a zirconia bowl (10 mL) with about 3 mL of zirconia balls (2 mm in diameter) and mixed by a vibratory mill MM 400 (Retsch). The first grinding process of the educts lasted 30 min at a frequency of 30 Hz. Next, 0.1 g of h-PMMA and different amounts (0, 0.01, 0.015, 0.02, 0.025, and 0.03 g) of PEI-25K were dissolved in 5 mL of DCM and added to the milling jar. The milling process was continued for another 30 min resulting in the formation of the NPs. Next, the mixture was diluted with 5 mL of DCM and centrifuged for 5 min at 5,000 rpm. The supernatant containing the NPs was collected, and the NPs were destabilized by adding n-hexane. The resulting suspension was centrifuged at 5,000 rpm for 5 min. The precipitate was re-dissolved in 10 mL of toluene for further characterization and processing. For anion exchange, 0.1 M solutions of ZnCl$_2$ or ZnI$_2$ in CH$_3$OH were used to treat the original h-PMMA/PEI-stabilized green-emitting NPs. The OLA/OA-coordinated CsPbBr$_3$ NPs (as a reference sample for the stability test) were prepared by the hot injection method in exact accordance with the literature [52, 53].

4.2 Centrifugal purification of perovskite nanoparticles

High-speed centrifugation could be used to additionally purify the NPs. Specifically, the as-prepared NPs in toluene were centrifuged at 10,000 rpm for 5 min to collect supernatant. The excessive polymer was removed by further high-speed centrifugation with 13,000 rpm for 15 min. The precipitate was collected and re-dissolved in pure toluene.

4.3 Test of anti-methanol stability and durability

An equal volume of methanol was added to the toluene solution of NPs to test its stability against polar solvents. For PL measurements, the NPs solution in the control group was directly diluted twice with toluene. For the durability test of the NPs capped by h-PMMA/PEI, excessive n-hexane was used to precipitate the NPs dissolved in toluene. The precipitate was redispersed into the same amount of toluene as initially used. The above precipitation/redispersion steps were repeated several times. For testing the durability of OLA/OA-capped NPs, a 3-fold volume of ethyl acetate was added to the toluene solution to precipitate the NPs, followed by centrifugation at 10,000 rpm for 5 min. The precipitate was redispersed into the same amount of toluene as initially used. The above precipitation/ redispersion steps were repeated several times.

4.4 Optical gain measurements

Before preparing the NP films for the ASE testing, excess polymer in the resulting h-PMMA/PEI-capped NPs was removed based on the above purification steps. After purification and

high-speed centrifugation, the precipitate was dissolved in a small amount of toluene and then deposited on quartz glass (1 cm × 1 cm) to obtain a film with a high density of emitting NPs. For ASE measurements, we used pulses from a Ti:Sapphire laser amplifier (Spitfire, Spectra Physics) with a pulse width of ~ 110 fs at a pulse rate of 1 kHz and 800 nm wavelength. The wavelength was halved with a frequency-doubling nonlinear crystal, and the remaining 800 nm excitation was filtered out via a short-pass filter. The incoming 400 nm pulses were passed through a cylindrical lens to obtain a stripe excitation. The sample was positioned at the focal point of the cylindrical lens and oriented normally to the pump. The emission was collected from the edge of the sample with an optical fiber coupled to a spectrometer (Maya 2000, Ocean Optics). For VSL measurement, a slit with variable width was placed right before the sample to control the length of the excitation stripe.

Acknowledgements

Electronic Supplementary Material: Supplementary material (chemicals, characterization method, TEM images, EDX data, element distribution map, lattices marks, scheme of the grinding process, tyndall experiment, DLS result, control experiments, images of blue/red perovskite NPs, and photostability figures) is available in the online version of this article at https://doi.org/10.1007/s12274-020-3152-7.

References

[1] Kovalenko, M. V.; Protesescu, L.; Bodnarchuk, M. I. Properties and potential optoelectronic applications of lead halide perovskite nanocrystals. *Science* **2017**, *358*, 745–750.

[2] Yan, F.; Tan, S. T.; Li, X.; Demir, H. V. Light generation in lead halide perovskite nanocrystals: LEDs, color converters, lasers, and other applications. *Small* **2019**, *15*, 1902079.

[3] Lin, K. B.; Xing, J.; Quan, L. N.; de Arquer, F. P. G.; Gong, X. W.; Lu, J. X.; Xie, L. Q.; Zhao, W. J.; Zhang, D.; Yan, C. Z. et al. Perovskite light-emitting diodes with external quantum efficiency exceeding 20 percent. *Nature* **2018**, *562*, 245–248.

[4] Yan, F.; Xing, J.; Xing, G. C.; Quan, L.; Tan, S. T.; Zhao, J. X.; Su, R.; Zhang, L. L.; Chen, S.; Zhao, Y. W. et al. Highly efficient visible colloidal lead-halide perovskite nanocrystal light-emitting diodes. *Nano Lett.* **2018**, *18*, 3157–3164.

[5] Zhou, Q. C.; Bai, Z. L.; Lu, W. G.; Wang, Y. T.; Zou, B. S.; Zhong, H. Z. *In situ* fabrication of halide perovskite nanocrystal-embedded polymer composite films with enhanced photoluminescence for display backlights. *Adv. Mater.* **2016**, *28*, 9163–9168.

[6] Chen, X. M.; Zhang, F.; Ge, Y.; Shi, L. F.; Huang, S.; Tang, J. L.; Lv, Z.; Zhang, L.; Zou, B. S.; Zhong, H. Z. Centimeter-sized Cs_4PbBr_6 crystals with embedded $CsPbBr_3$ nanocrystals showing superior photoluminescence: Nonstoichiometry induced transformation and light-emitting applications. *Adv. Funct. Mater.* **2018**, *28*, 1706567.

[7] Xu, Y. Q.; Chen, Q.; Zhang, C. F.; Wang, R.; Wu, H.; Zhang, X. Y.; Xing, G. C.; Yu, W. W.; Wang, X. Y.; Zhang, Y. et al. Two-photon-pumped perovskite semiconductor nanocrystal lasers. *J. Am. Chem. Soc.* **2016**, *138*, 3761–3768.

[8] Wang, Y.; Yu, D. J.; Wang, Z.; Li, X. M.; Chen, X. X.; Nalla, V.; Zeng, H. B.; Sun, H. D. Solution-grown $CsPbBr_3/Cs_4PbBr_6$ perovskite nanocomposites: Toward temperature-insensitive optical gain. *Small* **2017**, *13*, 1701587.

[9] Chen, Q. S.; Wu, J.; Ou, X. Y.; Huang, B. L.; Almutlaq, J.; Zhumekenov, A. A.; Guan, X. W.; Han, S. Y.; Liang, L. L.; Yi, Z. G. et al. All-inorganic perovskite nanocrystal scintillators. *Nature* **2018**, *561*, 88–93.

[10] Zhang, Y. H.; Sun, R. J.; Ou, X. Y.; Fu, K. F.; Chen, Q. S.; Ding, Y. C.; Xu, L. J.; Liu, L. M.; Han, Y.; Malko, A. V. et al. Metal halide perovskite nanosheet for X-ray high-resolution scintillation imaging screens. *ACS Nano* **2019**, *13*, 2520–2525.

[11] Huang, H.; Bodnarchuk, M. I.; Kershaw, S. V.; Kovalenko, M. V.; Rogach, A. L. Lead halide perovskite nanocrystals in the research spotlight: Stability and defect tolerance. *ACS Energy Lett.* **2017**, *2*, 2071–2083.

[12] Kang, J.; Wang, L. W. High defect tolerance in lead halide perovskite $CsPbBr_3$. *J. Phys. Chem. Lett.* **2017**, *8*, 489–493.

[13] Akkerman, Q. A.; Rainò, G.; Kovalenko, M. V.; Manna, L. Genesis, challenges and opportunities for colloidal lead halide perovskite nanocrystals. *Nat. Mater.* **2018**, *17*, 394–405.

[14] Krieg, F.; Ochsenbein, S. T.; Yakunin, S.; Ten Brinck, S.; Aellen, P.; Suess, A.; Clerc, B.; Guggisberg, D.; Nazarenko, O.; Shynkarenko, Y. et al. Colloidal $CsPbX_3$ (X = Cl, Br, I) nanocrystals 2.0: Zwitterionic capping ligands for improved durability and stability. *ACS Energy Lett.* **2018**, *3*, 641–646.

[15] Yang, D. D.; Li, X. M.; Zhou, W. H.; Zhang, S. L.; Meng, C. F.; Wu, Y.; Wang, Y.; Zeng, H. B. $CsPbBr_3$ quantum dots 2.0: Benzenesulfonic acid equivalent ligand awakens complete purification. *Adv. Mater.* **2019**, *31*, 1900767.

[16] Zheng, W. L.; Li, Z. C.; Zhang, C. Y.; Wang, B.; Zhang, Q. G.; Wan, Q.; Kong, L.; Li, L. Stabilizing perovskite nanocrystals by controlling protective surface ligands density. *Nano Res.* **2019**, *12*, 1461–1465.

[17] Li, Y.; Wang, X. Y.; Xue, W. N.; Wang, W.; Zhu, W.; Zhao, L. J. Highly luminescent and stable $CsPbBr_3$ perovskite quantum dots modified by phosphine ligands. *Nano Res.* **2019**, *12*, 785–789.

[18] Pan, J.; Shang, Y. Q.; Yin, J.; De Bastiani, M.; Peng, W.; Dursun, I.; Sinatra, L.; El-Zohry, A. M.; Hedhili, M. N.; Emwas, A. H. et al. Bidentate ligand-passivated CsPbI₃ perovskite nanocrystals for stable near-unity photoluminescence quantum yield and efficient red light-emitting diodes. *J. Am. Chem. Soc.* **2018**, *140*, 562–565.

[19] Lu, C.; Li, H.; Kolodziejski, K.; Dun, C. C.; Huang, W. X.; Carroll, D.; Geyer, S. M. Enhanced stabilization of inorganic cesium lead triiodide (CsPbI₃) perovskite quantum dots with tri-octylphosphine. *Nano Res.* **2018**, *11*, 762–768.

[20] Xue, W. N.; Wang, X. Y.; Wang, W.; He, F. F.; Zhu, W.; Li, Y. Aluminum distearate-modified CsPbX₃ (X = I, Br, or Cl/Br) nanocrystals with enhanced optical and structural stabilities. *CCS Chem.* **2020**, *2*, 13–23.

[21] Song, W. T.; Wang, Y. M.; Wang, B.; Yao, Y. F.; Wang, W. G.; Wu, J. H.; Shen, Q.; Luo, W. J.; Zou, Z. G. Super stable CsPbBr₃@SiO₂ tumor imaging reagent by stress-response encapsulation. *Nano Res.* **2020**, *13*, 795–801.

[22] Yuan, S.; Chen, D. Q.; Li, X. Y.; Zhong, J. S.; Xu, X. H. *In situ* crystallization synthesis of CsPbBr₃ perovskite quantum dot-embedded glasses with improved stability for solid-state lighting and random upconverted lasing. *ACS Appl. Mater. Interfaces* **2018**, *10*, 18918–18926.

[23] Pan, A. Z.; Wang, J. L.; Jurow, M. J.; Jia, M. J.; Liu, Y.; Wu, Y. S.; Zhang, Y. F.; He, L.; Liu, Y. General strategy for the preparation of stable luminous nanocomposite inks using chemically addressable CsPbX₃ peroskite nanocrystals. *Chem. Mater.* **2018**, *30*, 2771–2780.

[24] Li, Z. C.; Kong, L.; Huang, S. Q.; Li, L. Highly luminescent and ultrastable CsPbBr₃ perovskite quantum dots incorporated into a silica/alumina monolith. *Angew. Chem., Int. Ed.* **2017**, *56*, 8134–8138.

[25] Huang, H.; Chen, B. K.; Wang, Z. G.; Hung, T. F.; Susha, A. S.; Zhong, H. Z.; Rogach, A. L. Water resistant CsPbX₃ nanocrystals coated with polyhedral oligomeric silsesquioxane and their use as solid state luminophores in all-perovskite white light-emitting devices. *Chem. Sci.* **2016**, *7*, 5699–5703.

[26] Raja, S. N.; Bekenstein, Y.; Koc, M. A.; Fischer, S.; Zhang, D. D.; Lin, L. W.; Ritchie, R. O.; Yang, P. D.; Alivisatos, A. P. Encapsulation of perovskite nanocrystals into macroscale polymer matrices: Enhanced stability and polarization. *ACS Appl. Mater. Interfaces* **2016**, *8*, 35523–35533.

[27] de Weerd, C.; Lin, J. H.; Gomez, L.; Fujiwara, Y.; Suenaga, K.; Gregorkiewicz, T. Hybridization of single nanocrystals of Cs₄PbBr₆ and CsPbBr₃. *J. Phys. Chem. C* **2017**, *121*, 19490–19496.

[28] Chen, Y. M.; Zhou, Y.; Zhao, Q.; Zhang, J. Y.; Ma, J. P.; Xuan, T. T.; Guo, S. Q.; Yong, Z. J.; Wang, J.; Kuroiwa, Y. et al. Cs₄PbBr₆/CsPbBr₃ perovskite composites with near-unity luminescence quantum yield: Large-scale synthesis, luminescence and formation mechanism, and white light-emitting diode application. *ACS Appl. Mater. Interfaces* **2018**, *10*, 15905–15912.

[29] Jia, C.; Li, H.; Meng, X. W.; Li, H. B. CsPbX₃/Cs₄PbX₆ core/shell perovskite nanocrystals. *Chem. Commun.* **2018**, *54*, 6300–6303.

[30] Zhu, B. S.; Li, H. Z.; Ge, J.; Li, H. D.; Yin, Y. C.; Wang, K. H.; Chen, C.; Yao, J. S.; Zhang, Q.; Yao, H. B. Room temperature precipitated dual phase CsPbBr₃-CsPb₂Br₅ nanocrystals for stable perovskite light emitting diodes. *Nanoscale* **2018**, *10*, 19262–19271.

[31] He, M.; Wang, C. Y.; Li, J. Z.; Wu, J.; Zhang, S. W.; Kuo, H. C.; Shao, L. Y.; Zhao, S. C.; Zhang, J. Z.; Kang, F. Y. et al. CsPbBr₃-Cs₄PbBr₆ composite nanocrystals for highly efficient pure green light emission. *Nanoscale* **2019**, *11*, 22899–22906.

[32] Lou, S. Q.; Zhou, Z.; Xuan, T. T.; Li, H. L.; Jiao, J.; Zhang, H. W.; Gautier, R.; Wang, J. Chemical transformation of lead halide perovskite into insoluble, less cytotoxic, and brightly luminescent CsPbBr₃/CsPb₂Br₅ composite nanocrystals for cell imaging. *ACS Appl. Mater. Interfaces* **2019**, *11*, 24241–24246.

[33] Nenon, D. P.; Pressler, K.; Kang, J.; Koscher, B. A.; Olshansky, J. H.; Osowiecki, W. T.; Koc, M. A.; Wang, L. W.; Alivisatos, A. P. Design principles for trap-free CsPbX₃ nanocrystals: Enumerating and eliminating surface halide vacancies with softer lewis bases. *J. Am. Chem. Soc.* **2018**, *140*, 17760–17772.

[34] Akkerman, Q. A.; Abdelhady, A. L.; Manna, L. Zero-dimensional cesium lead halides: History, properties, and challenges. *J. Phys. Chem. Lett.* **2018**, *9*, 2326–2337.

[35] Wang, L. L.; Liu, H.; Zhang, Y. H.; Mohammed, O. F. Photoluminescence origin of zero-dimensional Cs₄PbBr₆ perovskite. *ACS Energy Lett.* **2020**, *5*, 87–99.

[36] Jiang, G. C.; Guhrenz, C.; Kirch, A.; Sonntag, L.; Bauer, C.; Fan, X. L.; Wang, J.; Reineke, S.; Gaponik, N.; Eychmüller, A. Highly luminescent and water-resistant CsPbBr₃-CsPb₂Br₅ perovskite nanocrystals coordinated with partially hydrolyzed poly(methyl methacrylate) and polyethylenimine. *ACS Nano* **2019**, *13*, 10386–10396.

[37] Kerner, R. A.; Schloemer, T. H.; Schulz, P.; Berry, J. J.; Schwartz, J.; Sellinger, A.; Rand, B. P. Amine additive reactions induced by the soft lewis acidity of Pb²⁺ in halide perovskites. Part I: Evidence for Pb–alkylamide formation. *J. Mater. Chem. C* **2019**, *7*, 5251–5259.

[38] Palazon, F.; El Ajjouri, Y.; Sebastia-Luna, P.; Lauciello, S.; Manna, L.; Bolink, H. J. Mechanochemical synthesis of inorganic halide perovskites: Evolution of phase-purity, morphology, and photoluminescence. *J. Mater. Chem. C* **2019**, *7*, 11406–11410.

[39] Jana, A.; Mittal, M.; Singla, A.; Sapra, S. Solvent-free, mechanochemical syntheses of bulk trihalide perovskites and their nanoparticles. *Chem. Commun.* **2017**, *53*, 3046–3049.

[40] Liu, Y. J.; Wang, Z. W.; Liang, S.; Li, Z. L.; Zhang, M. Y.; Li, H. M.; Lin, Z. Q. Polar organic solvent-tolerant perovskite nanocrystals permanently ligated with polymer hairs via star-like molecular bottlebrush trilobe nanoreactors. *Nano Lett.* **2019**, *19*, 9019–9028.

[41] Yoon, Y. J.; Chang, Y. J.; Zhang, S. G.; Zhang, M.; Pan, S.; He, Y. J.; Lin, C. H.; Yu, S. T.; Chen, Y. H.; Wang, Z. W. et al. Enabling tailorable optical properties and markedly enhanced stability of perovskite quantum dots by permanently ligating with polymer hairs. *Adv. Mater.* **2019**, *31*, 1901602.

[42] Udayabhaskararao, T.; Kazes, M.; Houben, L.; Lin, H.; Oron, D. Nucleation, growth, and structural transformations of perovskite nanocrystals. *Chem. Mater.* **2017**, *29*, 1302–1308.

[43] Kerner, R. A.; Schloemer, T. H.; Schulz, P.; Berry, J. J.; Schwartz, J.; Sellinger, A.; Rand, B. P. Amine additive reactions induced by the soft lewis acidity of Pb²⁺ in halide perovskites. Part II: Impacts of amido Pb impurities in methylammonium lead triiodide thin films. *J. Mater. Chem. C* **2019**, *7*, 5244–5250.

[44] Guo, Y. L.; Shoyama, K.; Sato, W.; Nakamura, E. Polymer stabilization of lead(II) perovskite cubic nanocrystals for semitransparent solar cells. *Adv. Energy Mater.* **2016**, *6*, 1502317.

[45] Kurahashi, N.; Mizuno, H.; Sasaki, F.; Yanagi, H. Whispering gallery mode lasing from CH₃NH₃PbBr₃/PEO composites grown in a microcapillary. *J. Phys. Chem. C* **2020**, *124*, 3242–3249.

[46] Akkerman, Q. A.; D'Innocenzo, V.; Accornero, S.; Scarpellini, A.; Petrozza, A.; Prato, M.; Manna, L. Tuning the optical properties of cesium lead halide perovskite nanocrystals by anion exchange reactions. *J. Am. Chem. Soc.* **2015**, *137*, 10276–10281.

[47] Guhrenz, C.; Benad, A.; Ziegler, C.; Haubold, D.; Gaponik, N.; Eychmüller, A. Solid-state anion exchange reactions for color tuning of CsPbX₃ Perovskite nanocrystals. *Chem. Mater.* **2016**, *28*, 9033–9040.

[48] Liu, H.; Siron, M.; Gao, M. Y.; Lu, D.; Bekenstein, Y.; Zhang, D. D.; Dou, L. T.; Alivisatos, A. P.; Yang, P. D. Lead halide perovskite nanowires stabilized by block copolymers for Langmuir-Blodgett assembly. *Nano Res.* **2020**, *13*, 1453–1458.

[49] Shaklee, K. L.; Leheny, R. F. Direct determination of optical gain in semiconductor crystals. *Appl. Phys. Lett.* **1971**, *18*, 475–477.

[50] Shaklee, K. L.; Nahory, R. E.; Leheny, R. F. Optical gain in semiconductors. *J. Lumin.* **1973**, *7*, 284–309.

[51] Wei, Q.; Li, X. J.; Liang, C.; Zhang, Z. P.; Guo, J.; Hong, G.; Xing, G. C.; Huang, W. Recent progress in metal halide perovskite micro- and nanolasers. *Adv. Opt. Mater.* **2019**, *7*, 1900080.

[52] Protesescu, L.; Yakunin, S.; Bodnarchuk, M. I.; Krieg, F.; Caputo, R.; Hendon, C. H.; Yang, R. X.; Walsh, A.; Kovalenko, M. V. Nanocrystals of cesium lead halide perovskites (CsPbX₃, X = Cl, Br, and I): Novel optoelectronic materials showing bright emission with wide color gamut. *Nano Lett.* **2015**, *15*, 3692–3696.

[53] Chen, Z. J.; Hu, Y. G.; Wang, J.; Shen, Q.; Zhang, Y. H.; Ding, C.; Bai, Y.; Jiang, G. C.; Li, Z. Q.; Gaponik, N. Boosting photocatalytic CO₂ reduction on CsPbBr₃ perovskite nanocrystals by immobilizing metal complexes. *Chem. Mater.* **2020**, *32*, 1517–1525.